Progress in Additive Manufacturing
https://doi.org/10.1007/s40964-025-01288-x

FULL RESEARCH ARTICLE

Impact of different pore types on the tensile and fatigue properties of AlSi10Mg parts produced by laser powder bed fusion

Steffen Kramer[1,2] · Helena Wexel[2] · Anisa Purwitasari[2] · Michael Jarwitz[1] · Volker Schulze[2] · Frederik Zanger[2]

Received: 31 October 2024 / Accepted: 27 July 2025

Abstract
The mechanical properties of laser powder bed fusion (PBF-LB) parts such as fatigue strength or tensile strength are greatly influenced by the porosity occurring in the material. While it is common to achieve relative densities over 99.5% for the aluminum alloy AlSi10Mg, in practice, the formation of statistically occurring oxide pores cannot be avoided completely. Due to their irregular shape, these pores are detrimental for the mechanical properties. It is hypothesized that oxide pores can be avoided by increasing the energy input. This in turn leads to the formation of spherical keyhole pores. However, it is not sufficiently understood how keyhole porosity affects the mechanical properties with regard to oxide pores. Therefore, this work investigates the impact of keyhole pores, lack of fusion pores and oxide pores on the mechanical properties of PBF-LB AlSi10Mg parts. Results show the importance of single critical defects for the fatigue behavior compared to the impact of relative porosity and reveal the less detrimental nature of keyhole pores compared to oxide pores. Despite a much higher relative porosity, the tensile strength of specimens containing keyhole pores is comparable to that of highly dense parts whereas the fatigue strength has even improved.

Keywords Powder bed fusion · AlSi10Mg · Keyhole pores · Oxide pores · Tensile strength · Fatigue

1 Introduction

Laser powder bed fusion (PBF-LB) is nowadays an established industrial process for manufacturing lightweight metal parts with complex shapes. While it is widely used for tool and medical applications, the use for automotive and aerospace applications is still hindered by the lack of technological knowledge of the behavior of load bearing PBF-LB parts. [1] Mechanical properties of PBF-LB parts, especially fatigue behavior, differ significantly from cast or wrought parts due to typical process-related characteristics, such as rough surfaces, heterogeneous microstructure, and various pore defects [2–5].

The aluminum alloy AlSi10Mg is widely used for PBF-LB parts in automotive and aerospace applications due to its high specific strength, good processability in PBF-LB, and low shrinkage [6]. In recent years, numerous studies aimed to improve the understanding of the impact of AlSi10Mg PBF-LB part characteristics on the mechanical properties. The current progress on this topic is well summarized in several review publications [7–9]. The impact of surface roughness and microstructure on the tensile strength [10] and fatigue strength [1, 11–14] is well understood for this material. Nicoletto [15] for example specifically investigated the influence of the surface finish on the fatigue properties. Sajadi et al. [16] showed that heat treatments can be beneficial for the fatigue strength and crack propagation characteristics of AlSi10Mg PBF-LB parts. Beretta et al. [17] proved that experimental results of fatigue strength investigations of AlSi10Mg PBF-LB parts are transferable to actual components. However, numerous studies conclude that pore defects have a major effect on the mechanical properties and in particular on the fatigue strength [18–20]. Afroz et al. [21] showed in a recent experimental study that for a surface roughness Ra < 1 µm, pore defects become the controlling factor for the fatigue properties. Experiments by Sausto et al. [22] demonstrated that the resulting stress acting at critical defects is depending on the local residual stress in the material. In a comprehensive study, Strauß et al. [23] compared

✉ Steffen Kramer
steffen.kramer@ifsw.uni-stuttgart.de

1 Institut fuer Strahlwerkzeuge IFSW, University of Stuttgart, Pfaffenwaldring 43, 70569 Stuttgart, Germany

2 wbk Institute of Production Science, Karlsruhe Institute of Technology, Kaiserstraße 12, 76131 Karlsruhe, Germany

Published online: 06 August 2025

the effect of residual stress, surface roughness, and porosity on the fatigue life of AlSi10Mg PBF-LB parts, proving porosity to be a dominant factor for the fatigue properties.

Several studies have shown that for the PBF-LB process, a certain amount of porosity is inevitable [24–26]. There are different types of pore defects that can occur in the PBF process. Lack of fusion (LoF) pores form either due to insufficient heat input and thus incomplete melting of the powder or due to defects in the spreaded powder layer [27]. Keyhole (KH) pores often occur due to excessive heat input, e.g., at the end of scan vectors because of the dwell time of the laser beam [28, 29]. PBF-LB parts manufactured using the aluminum alloy AlSi10Mg can additionally contain hydrogen pores and oxide pores. Hydrogen pores form by agglomeration of hydrogen atoms in the melt pool. Hydrogen is either captured during the powder atomizing process or stems from moisture gathered during powder handling [30]. These pores are small (<5 … 30 µm in diameter), spherically shaped and have no significant impact on the mechanical properties [31–34]. During the PBF-LB process, the oxidation of aluminum with residual oxygen in the process chamber leads to the formation of an oxide layer on the melt surface and on previously solidified layers. Due to the high melting temperature of aluminum oxide, the oxide layer remains solid and acts as a separating layer which hinders the propagation of the melt pool. This leads to insufficient remelting of the previously solidified layers and adjacent scan tracks. As a result, cavities containing oxide layers remain between the melt pool, scan tracks, and previous layers. These oxide pores have an irregular shape and can reach several 100 µm in diameter [2, 35]. In numerous studies, oxide pores have been identified as critical ("killer") defects during fatigue testing of AlSi10Mg PBF-LB parts [36, 37]. Increased energy input during PBF-LB could break up the oxide layers to ensure sufficient bonding of the generated track to the previous layers but in turn gives rise to keyhole pore formation [35].

Different models were proposed to assess the impact of pore defects on the fatigue life. Murakami et al. proposed a method to measure the size of defects ($\sqrt{\text{area}}$) and calculate the respective stress intensity factors [38]. The El Haddad approach uses the $\sqrt{\text{area}}$-value to estimate the fatigue limit [39]. Experimental investigations with AlSi10Mg show good agreement with the proposed models [36, 40]. Based on these results, Strauß et al. [41] recently developed an equivalent stress model to analytically predict the fatigue life by including surface roughness and residual stress. Moreover, numerical models were proposed to assess the impact of pores on the fatigue behavior [42, 43]. However, all these investigations were carried out using only specimens with high relative densities and a minimal porosity consisting of oxide and hydrogen pores and under the assumption that high relative densities yield the best mechanical properties. Further, it is unclear if the proposed models [38, 39] are still valid for larger amounts of porosity. In an experimental study with the material Ti6Al4V, the impact of different amounts of LoF and KH porosity on tensile and fatigue strength was investigated. The results showed that LoF pores are much more harmful to the mechanical properties, whereas small amounts ($<1\%$) of KH only have a negligible impact. The analysis did not include the role of single critical defects, and moreover, oxide defects are not an issue when using titanium alloys in PBF-LB compared to aluminum alloys [34].

The present work therefore investigates the impact of keyhole pores on the mechanical properties of AlSi10Mg PBF-LB parts compared to the role of oxide defects and LoF defects. In a first step, specimens were manufactured using different process parameters and the resulting porosity configurations were analyzed. Tensile and fatigue tests are conducted and the critical defects leading to the failure of the fatigue specimens were analyzed in detail to assess the influence of different pore morphologies on the fatigue strength. The paper aims to underline the importance of fatigue properties, the superior role of single critical defects, and their size and shape compared to the overall porosity, which is currently commonly used as the central quality criterion.

2 Materials and methods

AlSi10Mg powder material with a powder size distribution of 20–63 µm, provided by m4p material solutions GmbH (Magdeburg, Germany), was used for the experiments. D_{10}, D_{50}, and D_{90} were measured with 30.71 µm, 42.14 µm, and 57.27 µm, respectively. The chemical composition of the material is given in Table 1.

For specimen production, an SLM 280 HL machine from Nikon SLM Solutions AG was used with a build plate size of 280×280 mm. The machine was equipped with one fiber laser source with a maximum power of 400 W and a wavelength of 1070 nm. The beam profile after the focusing optics was measured according to DIN EN ISO 11146–2 [44] giving a focus diameter of 83 µm, a Rayleigh length of 3.77 mm, and a M^2 of 1.33. Three different parameter sets (PS) were selected for specimen production for the tensile strength and fatigue strength tests. Parameter sets are given in Table 2. Layer thickness ($t=50$ µm) and hatch distance

Table 1 Material composition of AlSi10Mg powder material in %

Si	Mg	Fe	Mn	Ti	Zn	Cu	Al
9.8	0.35	0.18	0.01	0.03	0.01	<0.01	Bal

Table 2 Process parameter sets for specimen production

Parameter set (PS)	Characteristics	Laser power P in W	Scanning speed v in mm/s	Volumetric energy density VED = $\frac{P}{v \cdot t \cdot h}$ in J/mm^3
PS 1 "Standard/HD"	high density (HD)–standard PS	350	1150	35.8
PS 2 "KH"	Keyhole (KH) pores	350	550	74.9
PS 3 "LoF"	Lack of fusion (LoF) pores	200	950	24.8

($h = 170$ µm) were kept constant. A conventional stripe pattern was used as scanning pattern with a 67° rotation between every layer. The build plate temperature was kept constant at 100 °C for all specimens. Argon gas was used to ensure an inert atmosphere in the build chamber during the PBF-LB process.

Parameter set 1 (PS 1) is referred to as "standard/high density (HD)" as this represents the parameters recommended by the machine manufacturer with which it is possible to manufacture parts with maximum density. Results for the surface roughness and Woehler curve data for the standard/HD fatigue specimens are taken from the authors' own publication [45]; therefore, no HD fatigue specimens were manufactured exclusively for the present study. Parameter sets 2 and 3 were determined with an experimental parameter study and are meant to induce a substantial amount of porosity. PS 2 leads to the formation of spherical pores. Due to an excessive energy input by the laser beam, a fluctuating capillary or "keyhole" is formed in the melt pool. At the bottom of the capillary, shielding gas gets trapped and remains in the material as so-called "keyhole" (KH) pores [28]. PS 3 leads to "lack of fusion" (LoF) pores, which are the result of an insufficient energy input. These pores develop between two layers or two adjacent scan tracks as the melt pool does not sufficiently connect to the underlying or surrounding material. LoF pores are characterized by their irregular shape and the presence of unmolten powder particles in the cavity [32].

For tensile strength and fatigue strength measurements, geometries were designed according to DIN 50113 [46] and DIN 50125 [47]. Tensile testing specimens were manufactured horizontally. Cubic specimens with a size of $1 \times 1 \times 1$ cm^3 were manufactured along with the tensile specimens and were utilized to monitor the density and microstructure. To minimize the number of build jobs, all fatigue testing specimens were manufactured vertically. All tensile and fatigue specimens were manufactured in a cylindrical shape and subsequently machined to achieve the final geometries, as depicted in Fig. 1.

Density measurements on cubic and fatigue specimens were done via image evaluation of greyscale microscope images of ground and polished cross-sections. Five images were taken per specimen and converted into binary format. Porosity evaluations were carried out using the particle analysis tool provided by the image evaluation software (ImageJ, USA). A circularity threshold of 0.1 was used to exempt scratch marks from the evaluation. For the optical density measurement and porosity evaluation, an optical microscope was used (Keyence VHX-970 F, Germany). A scanning electron microscope (SEM) was used to further investigate the fracture surfaces (JEOL JSM-6010 LV, Germany). Vickers hardness was measured with a Qness "Q10A +" hardness testing system (ATM Qness GmbH, Germany). To avoid the influence of pores on the measured hardness, a micro-hardness measurement with a load of 1 N (equivalent to HV 0.1) was chosen which resulted in small indentations of around 40 µm in diameter.

Tensile tests were done using a tensile testing machine (Zwick Roell, Germany) with a maximum tensile force of 20 kN. Before testing, the specimen diameter was measured at three different positions and the mean diameter was used to calculate the stress value from the measured tensile force. The elongation at break was calculated by measuring the remaining plastic elongation of the fractured specimens. Five specimens were tested for every porosity configuration.

To assess the surface roughness of the machined fatigue specimens, the surface topography of every specimen was measured using a confocal microscope "µsurf custom" (nanofocus, Germany) prior to testing. An area of 1.6×1.6 mm^2 in the middle of the specimen was measured. After removing any outliers, the values of Sa (arithmetical mean height) and Sz (maximum height) were measured using the software µsoft analysis extended 7.4 (nanofocus, Germany). Fatigue strength was evaluated with a rotating bending test according to DIN 50100:2022–12 [48] ("pearl string method") with a stress ratio $R = -1$, a test frequency of 50 Hz, and a mean stress of 0 MPa. Specimens were tested in the high cycle fatigue range (load cycles 1E4–1E7) at several different loads. Specimens with more than 1E7 cycles were counted as run outs and were not included in the calculation of the Woehler curve which was calculated for a failure probability of 50%.

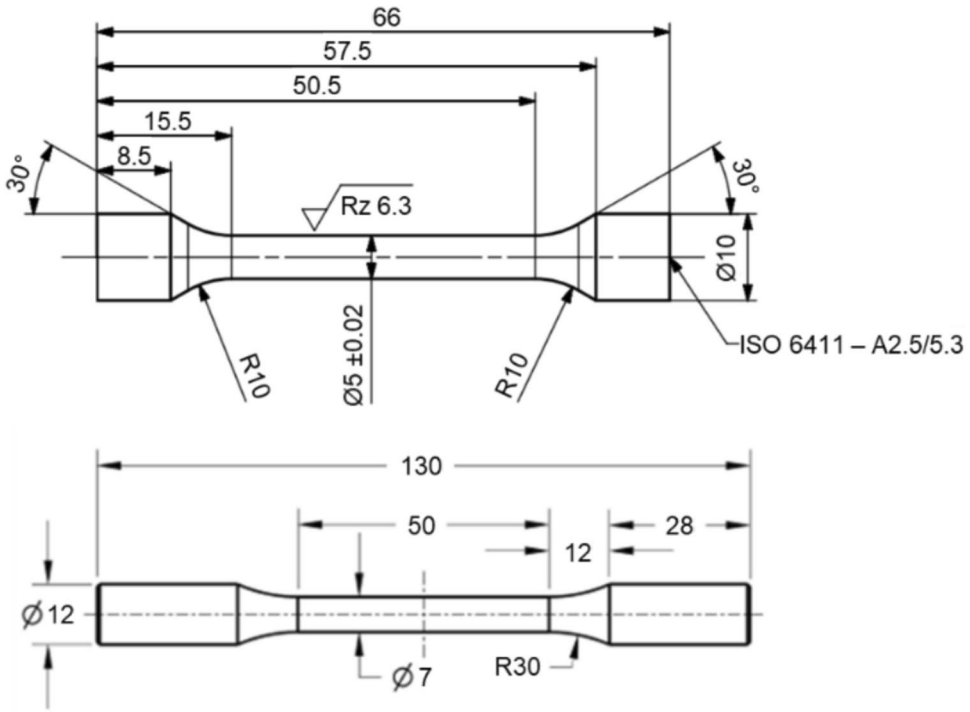

Fig. 1 Top: tensile test specimen geometry. Bottom: rotating bending test specimen geometry

3 Results and discussion

3.1 Porosity characterization

The porosity of each parameter set was evaluated on a cross-sectional area of one specimen of every pore configuration using at least three optical microscopy images per cross-section. Cross-sectional cuts were all prepared parallel to the build direction in the middle of the specimens. The porosity of the fatigue specimens was measured in the 1 cm at the top and bottom of the specimen and then averaged. The relative porosity as well as the average pore size and average circularity were measured for the characterization of the porosity. Representative images of the different pore morphologies are depicted in Fig. 2. The results of the porosity evaluation are summarized in Table 3. All images show the presence of small, spherical gas pores throughout the material. As small pores have a negligible impact on the mechanical properties [34], all pores < 100 µm^2 were exempted from the porosity characterization. The average pore circularity of the fatigue specimens is generally lower than that of the cubic specimens. Considering the standard deviation, the LoF and HD fatigue specimens show the same porosity and average pore size compared to the cubic specimens. The KH fatigue specimens show a lower porosity and lower average pore size compared to their cubic counterparts. Furthermore, the porosity of the LoF and HD fatigue specimens was the same for the top and bottom of the specimens. The KH fatigue specimens, however, showed a significantly lower porosity at the top

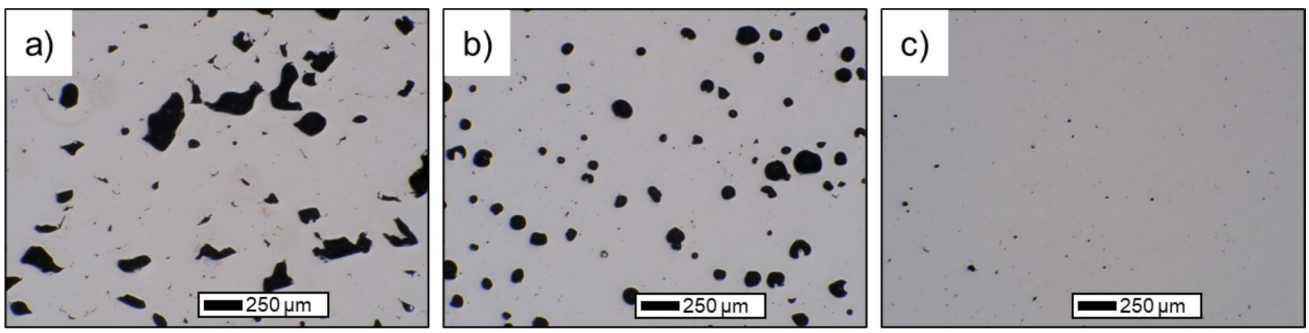

Fig. 2 Representative optical microscope images of polished cross-sections of cubic specimens with different porosities: **a** lack of fusion pores, **b** keyhole pores, and **c** highly dense specimen containing mostly hydrogen pores

Table 3 Characterization of the porosity configurations of the manufactured specimens

	Lack of fusion (LoF)		Keyhole (KH)		Standard/high density (HD)	
	Cubic specimens	Fatigue specimens	Cubic specimens	Fatigue specimens	Cubic specimens	Fatigue specimens
Av. pore size in μm^2 (Standard Deviation, SD)	5299 (354)	6768 (653)	3848 (352)	1966 (287)	326 (33)	486 (113)
Porosity (SD)	9.59% (0.28%)	10.35% (0.84%)	6.73% (0.84%)	2.06% (0.50%)	0.22% (0.04%)	0.20% (0.08%)
Av. circularity (SD)	0.536 (0.008)	0.569 (0.016)	0.776 (0.012)	0.752 (0.039)	0.654 (0.028)	0.656 (0.034)

(1.00 ± 0.45%) compared to the bottom part (3.05 ± 0.53%). It is at this point unclear why only the porosity of the KH fatigue specimens varies over the build height. The circularity of the KH pores remains unaffected by the change in porosity and is similar to that of the cubic specimens. Further, the porosity and pore size are for both, cubic and fatigue KH specimens, sorted between the LoF and HD specimens. As tensile and fatigue properties are assessed separately, this difference in porosity does not diminish the validity of the results.

The LoF pores have the largest average size and due to the irregular, mostly elongated shape the lowest average circularity. KH pores possess a near spherical shape and therefore have the highest circularity. The highly dense specimens contain only small pores, but based on the measured circularity, these pores seem to be more irregularly shaped compared to KH pores.

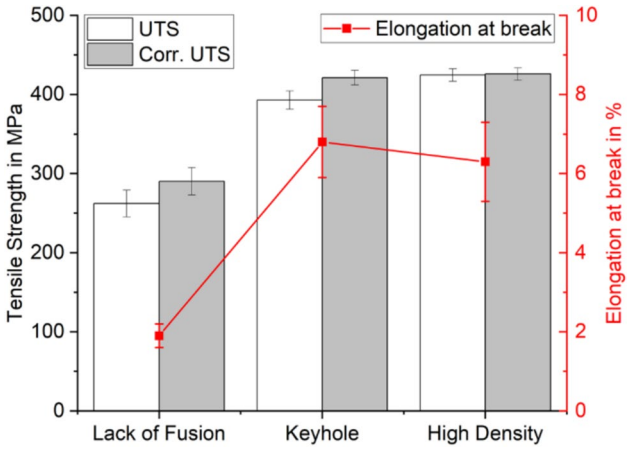

Fig. 3 Ultimate tensile strength (UTS), corrected UTS, and elongation at break for different porosity modifications. Error bars: standard deviation

3.2 Tensile tests

Tensile tests were performed to assess the influence of the pore morphology on the tensile strength of the material. The results of the tensile tests are depicted in Fig. 3. Detailed results are listed in Appendix A1. Based on the measured ultimate tensile strength (UTS), a corrected UTS was calculated assuming a linear rule of mixture for a composite material with one phase being null strength pores [33, 49]. The porosity values for the calculation are taken from Table 3. The LoF specimens reached the lowest UTS with 263 MPa and simultaneously the lowest elongation with only 1.9%. The UTS of the HD specimens reached 425 MPa at an average elongation of 6.3%, which is in good agreement with other published results for AlSi10Mg PBF-LB parts with high relative density [31, 50]. Despite the substantial porosity, the KH specimens reached a slightly lower UTS of 393 MPa and elongation of 6.8%. However, the corr. UTS of the KH specimens calculated with the linear rule of mixture and a porosity of 6.73% is equal to the corr. UTS of the HD specimens calculated with the respective porosity of 0.22%. The similar corr. UTS implies that the linear rule of mixture for materials with pores with high circularity (> 0.7) as presented in [33], can in this case still be applied for the UTS for a porosity of up to 6.73%. Therefore, it can be assumed that the present KH pores do not induce critical stress concentrations when compared with the HD specimens. As the corr. UTS of the LoF specimen is considerably lower, the LoF pores have a detrimental impact on the UTS and ductility due to high stress concentrations caused by their irregular shape.

The fracture surfaces of the tensile test specimens were investigated using scanning electron microscopy. Representative images of fracture surfaces of every pore morphology are shown in Fig. 4. The fracture surface of the LoF specimen is rough and dominated by large pores (Fig. 4a)) in which unmolten powder particles remained (Fig. 4d)). The KH specimen has a smoother fracture surface and shows numerous open spherical pores, indicating that the fracture passed through these pores. The fracture surface of the HD specimen contains only few small pores and a single macroscopic LoF defect with remaining powder particles. As it is the only LoF defect in the fracture surface and the HD material mostly contains small gas pores (see Fig. 2), it can be assumed that the LoF defect is not caused by insufficient

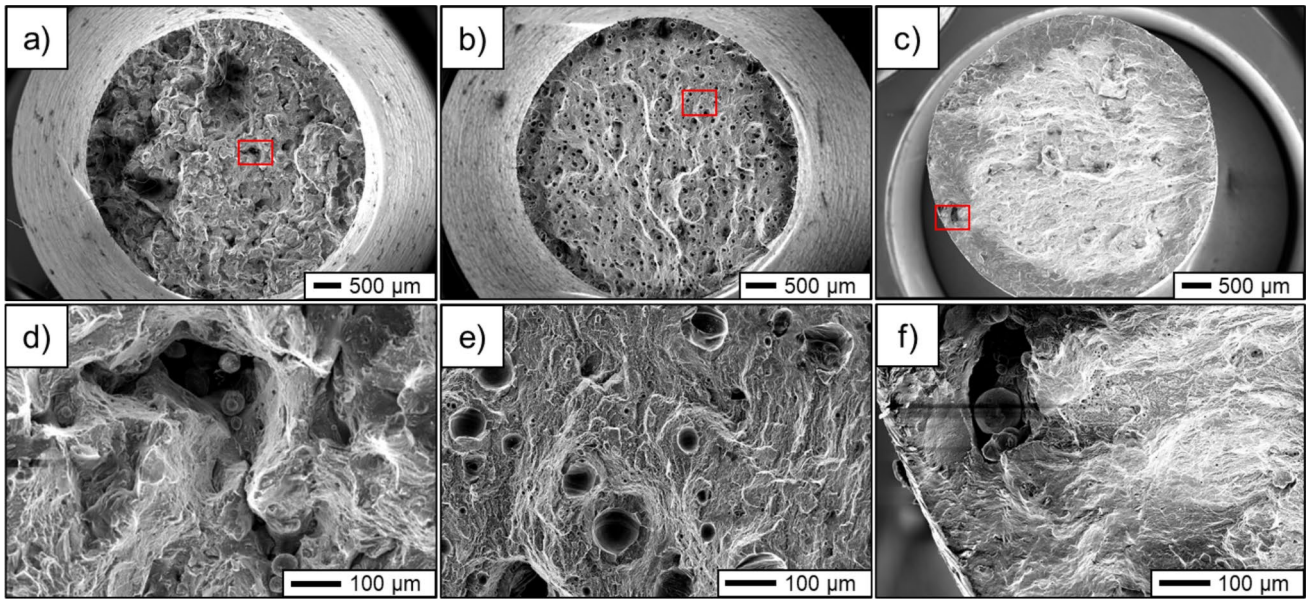

Fig. 4 SEM images of the fracture surfaces and enlarged sections with representative pore defects in the fracture surface: **a**, **d** lack of fusion specimen; **b**, **e** keyhole specimen; **c**, **f** standard specimen with oxide/lack of fusion defect

Table 4 Results of the surface roughness measurement of the fatigue test specimens

Specimen	Surface roughness Sa in µm
Standard (high density) [45]	1.15 (SD: 0.06)
Keyhole	1.41 (0.23)
Lack of fusion	3.84 (2.32)

energy input but by oxides (Fig. 4f)) and can therefore be classified as oxide pore.

3.3 Fatigue tests

Prior to the fatigue tests, the surface roughness of all fatigue specimens was measured using a confocal microscope. The results are summarized in Table 4.

Although all specimens were machined with the same settings, the Sa values differ significantly. This is caused by open pores on the machined specimen surface which affect the average surface roughness. As the LoF pores are larger, the average surface roughness is highest for the LoF specimen. Fatigue tests were performed on the rotating bending test machine according to the pearl string method. The results are summarized in Fig. 5 and Table 5. Detailed results are listed in Appendix A2. Results for the fatigue behavior of the highly dense standard material in Fig. 5 are taken from previously published work of the authors [45]. The LoF specimens clearly show the lowest fatigue strength, as no specimen exceeded 4E5 load cycles and the highest achieved

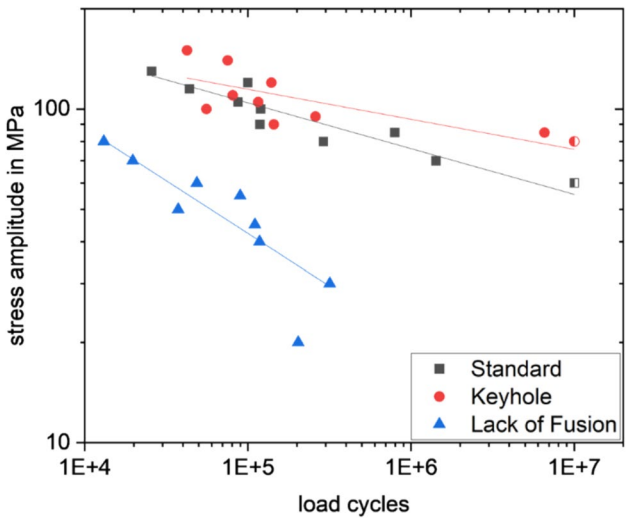

Fig. 5 Woehler curves in the high cycle fatigue (HCF) region for specimens with different pore types. Run outs are represented with half symbols. Woehler curve data for the Standard/HD specimens are taken from [45]

Table 5 Summary of the fit results of the Woehler curve ($y = a \bullet x^b$) in the HCF regime

Specimen	a	b	R^2
Standard (high density)	507.7	−0.14	0.87
Keyhole	323.3	−0.09	0.50
Lack of fusion	1601.1	−0.32	0.85

stress amplitude in the high cycle fatigue range (1E4–1E7 load cycles) was 80 MPa. The resulting slope of the Woehler curve is much steeper compared to the other curves. While the curves for HD and KH show a similar behavior for high stress amplitudes and low load cycle numbers, the curve of the KH specimens has an even lower slope and reached consequently a higher threshold at 80 MPa compared to 60 MPa for the HD specimens. Both stress amplitudes for run outs were confirmed with a second test. The single results for the KH specimens, however, exhibit a higher scatter ($R^2 = 0.50$) compared to the results of the HD specimens ($R^2 = 0.87$).

All fracture surfaces were investigated with an SEM to identify the crack-initiating defect as well as the fatigue fracture surface. Representative images for every porosity configuration are depicted in Fig. 6. The fracture surface of the LoF material is rough and multiple locations for crack initiation and propagation can be identified all around the circumference. The largest of these areas is depicted in Fig. 6d) showing multiple LoF pores as potentially critical defect. However, most of the fracture area is caused by the spontaneous crack propagation hinting at a short phase of stable crack propagation. This is supported by the findings of [27], showing that LoF defects are most likely interconnected when the relative density is < 95% enabling a spontaneous crack propagation. For most of the KH specimens, the critical defect was a keyhole pore at or near the surface (see Fig. 6e)). All of the HD specimens showed that crack propagation started at irregularly shaped pores at the specimen surface, which corresponds well with other investigations [36, 40, 51, 52].

The fracture surfaces of HD and KH specimens both consist of three different zones (Fig. 7) as defined by [12]. In the first zone (I), the fracture surface is smooth as small striations were presumably leveled again during single

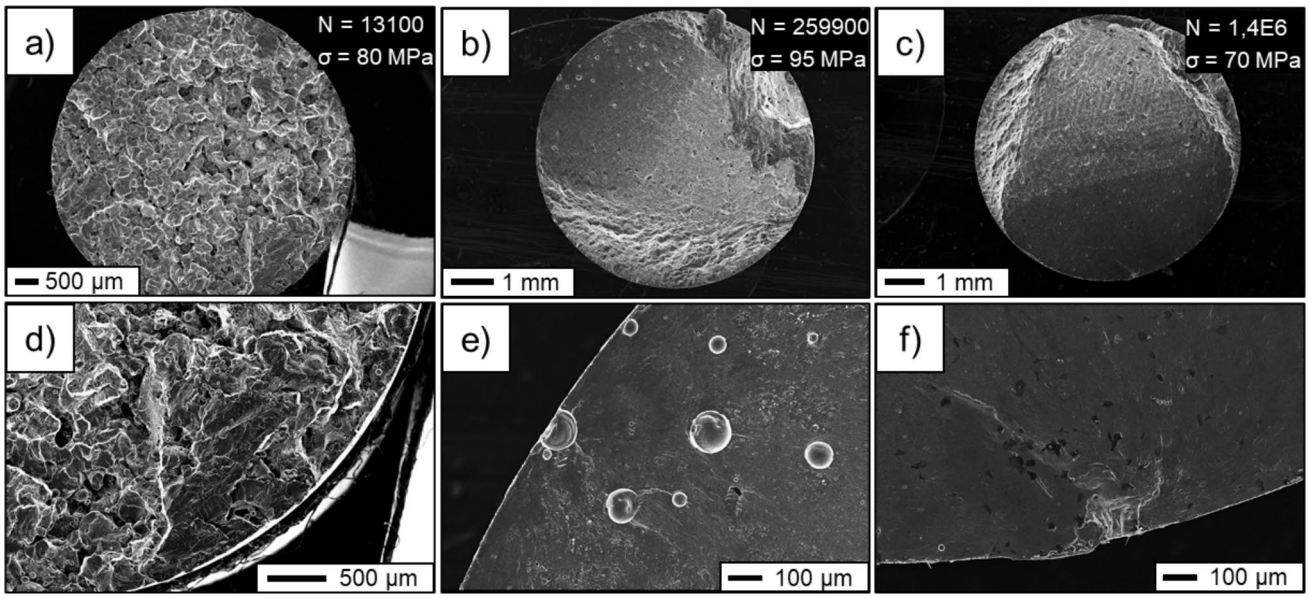

Fig. 6 Representative SEM images of fatigue fracture surfaces (top) and the critical crack-initiating defect (bottom) **a**, **d** Lack of fusion specimen; **b**, **e** keyhole specimen; **c**, **f** highly dense specimen

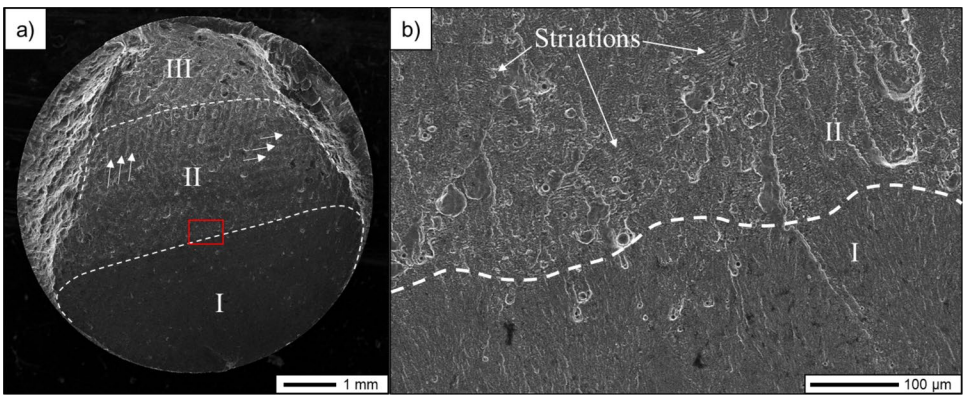

Fig. 7 **a** Different zones of crack propagations: (I) slow crack propagation, (II) fast crack propagation, and (III) overload fracture area. **b** Transition zone from slow to fast crack propagation

load changes. This hints at a slow crack propagation speed. The crack in zone (I) is oriented perfectly perpendicular to the direction of the bending stress. The size of zone (I) is inversely proportional to the applied stress amplitude. In zone (II), the fracture surface is rougher and striations (Fig. 7b)) as well as single scan tracks (Fig. 7a)), white arrows) can be identified. The scan track structure becomes more significant as the crack progresses, indicating that the crack propagation in zone (II) leading up to failure mostly follows the scan track borders. Multiple investigations showed that the scan track borders can form weak points in the material due to the coarse microstructure [53, 54]. The scan track structure in zone (II) is in general more prominent for the HD specimens than for the KH specimens. Due to the increased energy input during manufacturing, the melt pools of the KH specimens are considerably larger and deeper compared to the melt pools of the HD specimens. This circumstance could potentially hamper the crack propagation along the scan track borders in KH specimens. Zone (III) consists of the residual fracture surface. The direction of the crack propagation deviates and is no longer perpendicular to the specimen's rotation axis but points diagonally to the specimen surface.

3.4 Critical defect analysis of the fatigue tests

For every HD and KH specimen, the fracture surface was investigated and the critical defect from which the fatigue crack originated was identified. All critical defects were analyzed according to the method proposed by Murakami [38]. Since the LoF specimens showed much lower fatigue strength and no stable crack propagation, they are excluded from further investigation. In Fig. 8, examples of HD and KH specimens for the measurement of the size ($\sqrt{\text{area}}$) of critical defects are provided. In Fig. 8a, it is demonstrated that by following this method, the irregular shape of the pore defect is taken into account by measuring a larger area than the exact contour encloses.

For the HD specimens, most of the critical defects could be identified as oxide pores (Fig. 9). Oxide pores are described to possess an irregular shape and contain platelets originating from an oxide layer as well as aluminum droplets [37]. The same morphology and features can be identified in the image of the critical defect in Fig. 9 when comparing it to the results of Tang & Pistorius [37].

For the KH specimens, most of the critical defects were identified as keyhole pores. However, two KH specimens failed due to macroscopic lack of fusion pores (see

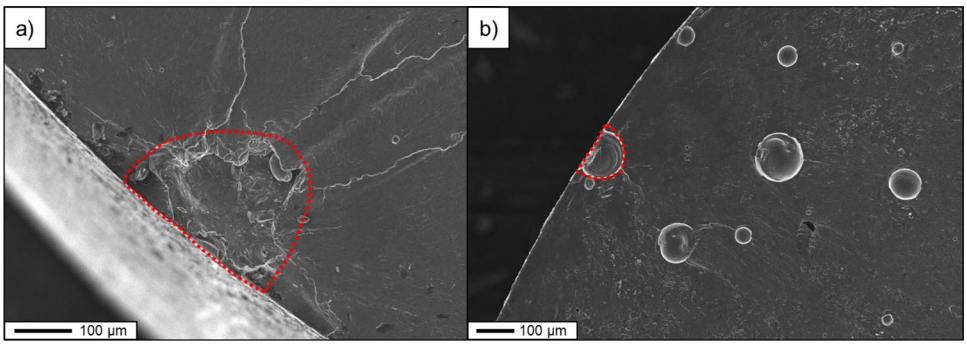

Fig. 8 Exemplary measurements of the size of critical defects according to the Murakami method. **a** Oxide pore in a highly dense specimen; **b** keyhole pore

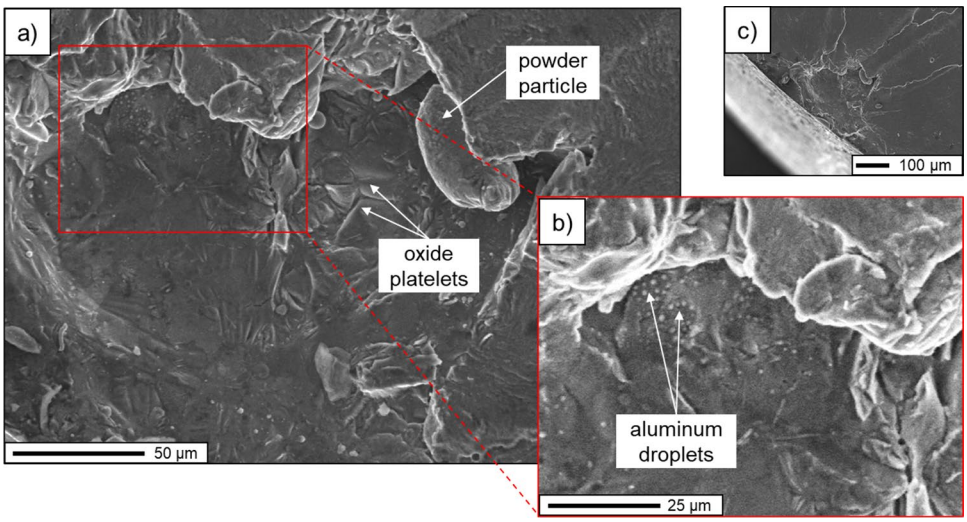

Fig. 9 **a** Close-up of a crack-initiating defect assumed to be an oxide pore as described in [37] containing oxide platelets and residual powder. **b** Detailed view of aluminum droplets. **c** Macroscopic view of the oxide pore

Fig. 10b)) and are from here on marked with open symbols in the following graphs. These two defects are believed to originate from irregularities during the recoating of the powder layer. A comparison of the defect size with the load cycles to failure shows that for the HD specimens, a smaller defect size correlates with a higher number of load cycles (Fig. 10a)). No such correlation could be found for specimens with keyhole defects. Comparing the pore morphology, it is evident that the critical defect for KH specimens is smaller and more circular than the critical defects of HD specimens (Fig. 10b)).

Based on the measurement of the defect size in accordance with the Murakami method, the $\sqrt{area}$-value allows the calculation of the stress intensity factor ΔK. As a result, the impact of the different pore morphologies can be quantified by calculating the stress intensity factor [38]

$$\Delta K = Y \cdot 2 \cdot \sigma_a \cdot \sqrt{\pi \sqrt{\text{area}}},$$

for every single defect, where σ_a is the stress amplitude, $\sqrt{area}$ is the size of the critical defect, and Y is the shape factor with a value of 0.65 for pores near or at the surface and 0.5 for internal pores [38]. Pores are classified as "near-surface" if the ratio of the radius of a circle with the same area as the critical defect divided by the distance of the center of the defect to the surface is > 0.8. As all critical defects are close to or at the surface, this is true for all investigated defects [38]. According to the presented criterium [55], none of the critical defects has to be classified as a pore cluster as the distance to adjacent pores in the fracture surface is sufficiently large.

The calculated values for ΔK are shown in Fig. 11. Although the KH specimens were tested with higher maximum stress amplitude, the maximum ΔK was calculated for the HD specimens. The keyhole defects lead to lower stress intensity factors due to the smaller $\sqrt{area}$ compared to the oxide pores in highly dense specimens.

The results of the defect analysis are summarized in a Kitagawa–Takahashi diagram [56] (Fig. 12). The fatigue limit defines the maximum stress level at which 1E7 load cycles (run out) or more can be performed without part failure. The fatigue limit of defect free specimens was estimated with 1.6 times the material hardness in HV [38]. With hardness values of 129 HV for the HD specimens and 123 HV for the KH specimens, the estimated fatigue limit is 206.4 MPa and 196.8 MPa, respectively. The long crack (LC) theory

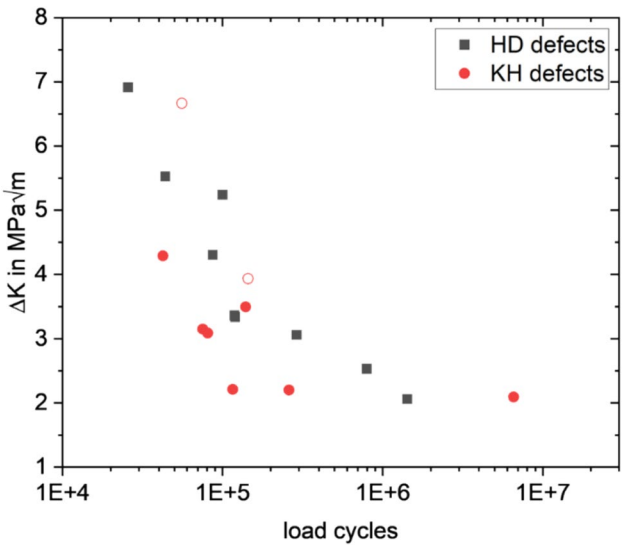

Fig. 11 Comparison of the stress intensity factor ΔK and the load cycles for the critical defects of "high-density (HD)" and "keyhole (KH)" specimens

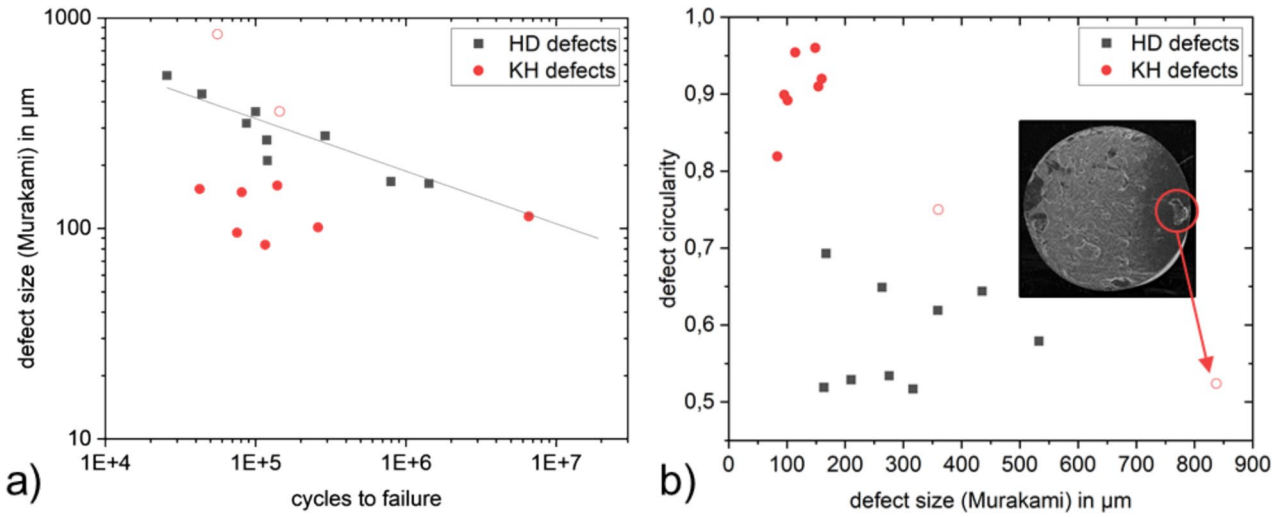

Fig. 10 Characterization of critical defects: **a** comparison of defect size and cycles to failure; **b** comparison of defect size and defect circularity

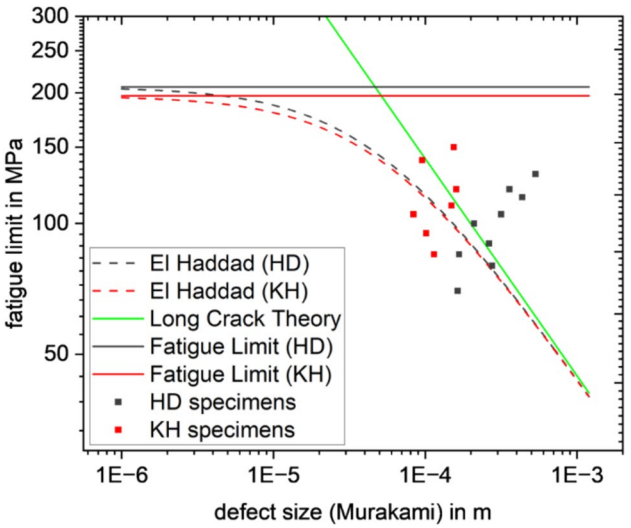

Fig. 12 Kitagawa–Takahashi diagram for the critical defects of "high-density (HD)" and "keyhole (KH)" AlSi10Mg material including the corresponding El-Haddad lines and calculated fatigue limits

considers the influence of defects and is determined by the material constant $\Delta K_{th\text{-}LC}$, which is given with 3.25 MPa$\sqrt{m}$ for AlSi10Mg processed with PBF-LB [36]. The intersection point with the fatigue limit gives the critical crack length a_0 which is 46.7 µm for HD specimens and 51.4 µm for KH specimens. The El Haddad approach describes the transition from fatigue limit estimation to LC theory by considering the effect of small cracks [39]. The resulting curve shows the predicted fatigue limit for a known defect size, which was determined by the Murakami method. Therefore, for a specific defect size, loads below the curve should lead to a run out and loads above the curve lead to part failure. As all specimens, for which the critical defects were identified, failed, all measurement points should be above the dashed line. Some results, however, fall below the curve predicted by the El Haddad approach. This could be attributed to tensile residual stresses induced by the machining process superimposing the testing stress amplitude as reported by [36]. The residual stress state depends on multiple factors of the PBF-LB and machining process and is unknown for the present specimens. However, considering the similar results for both specimen types, the accuracy of the model is apparently not affected by the substantial porosity of the KH specimens compared to the HD specimens. The presented results are limited to the failure-based fatigue behavior and do not allow any conclusion regarding the crack initiation and crack propagation leading up to the part failure. This could be subject of further research.

As seen in Fig. 6, the fatigue behavior of PBF-LB parts is determined by one single defect, at which the crack starts to grow. This defect is typically at or near the surface. The analysis of the critical defects shows that the size and shape of KH pores lead to a smaller $\sqrt{area}$ and, therefore, lower stress intensity factor and higher fatigue limit. This presumably leads to a delayed crack initiation for KH pores compared to oxide pores, which are the typical critical defect for HD specimens. Hence, the stress amplitude necessary to initiate a crack in the first place is also higher for KH pores resulting in the observed higher stress amplitude for the run-out specimen. This is supported by the slightly higher critical crack length a_0 for KH specimens compared to HD specimens. The El Haddad model predicting the fatigue limit based on a single critical defect fits for a substantial amount of keyhole porosity. This indicates that for this porosity configuration, the single defect still defines the fatigue behavior.

When comparing the present results with other experimental studies with similar boundary conditions, it becomes clear that many more factors determine the performance during fatigue testing. In the present study, the fatigue strength (amplitude) of the standard high-density specimens was measured at 60 MPa with an average critical defect size of 300 µm. Strauß et al. [36] also performed rotating bending fatigue tests which resulted in a fatigue strength of 100–110 MPa with a critical defect size of around 50–200 µm. Fini el al. [14], however, only measured a fatigue strength of 40 MPa for 1E6 load cycles instead of 1E7 load cycles. Liu et al. [57] reached a fatigue strength of 80 MPa with a critical defect size of around 100 µm. Even though the comparison of the different results shows in general a decrease of the fatigue strength with increasing critical defect size, there is still a significant amount of variance observable across the different studies Reasons for that could be different residual stress conditions, different microstructure, or surface roughness or the testing facility. This highlights the need for further research to quantify the impact of these different influencing factors. Nevertheless, the results clearly indicate that the fatigue behavior is significantly determined by single critical defects and their size.

The modeling of the fatigue behavior using the LC theory heavily relies on the value of material constant $\Delta K_{th\text{-}LC}$. The correct value, however, is not exactly known and is still disputed in the literature. While Strauß et al. [36] use 3.25 MPa$\sqrt{m}$ and achieved a good correlation with their experiments, they also proposed an adjusted value of 3.90 MPa$\sqrt{m}$. Other investigations recommend a value between 3.20 and 3.50 MPa$\sqrt{m}$ [58] or 3.60 MPa$\sqrt{m}$ [40]. For the present study, the LC theory using 3.25 MPa$\sqrt{m}$ fits quite well with the experimental results. It is, however,

clear that more investigations are needed to narrow down the correct value.

4 Conclusion

The aim of the present work was to investigate the impact of different amounts of porosity and pore morphology on the tensile and fatigue strength of AlSi10Mg parts produced by laser powder bed fusion. The main results are:

- While keyhole pores only have a small impact on the tensile properties with an UTS of 393 MPa compared to 425 MPa for highly dense specimens, lack of fusion pores disproportionally decrease the tensile strength due to their irregular shape leading to high stress concentrations.
- The fatigue behavior of parts with keyhole pores is not determined by the porosity but by a single critical defect from which the crack propagates.
- Highly dense AlSi10Mg PBF-LB parts often contain irregularly shaped oxide pores acting as critical defects and causing premature crack initiation.
- Due to the smaller size and spherical shape, keyhole pores are less likely to initiate a crack compared to oxide pores, and therefore, specimens with keyhole pores show an improved fatigue strength (80 MPa for 1E7 load cycles) compared to highly dense specimens with oxide pores (60 MPa for 1E7 load cycles).

It is, therefore, advisable to manufacture load bearing aluminum parts with a slightly excessive energy input to avoid the formation of oxide pores. These findings are especially relevant for the manufacturing of safety relevant and dynamically stressed parts in the aviation sector such as brackets or bearing clampings. Future work will be focused on optimizing the powder bed fusion process parameters to completely avoid the formation of oxide pores and simultaneously minimize the size of the more tolerable keyhole pores. Fatigue tests with specimens manufactured with optimized process parameters will demonstrate the potential of controlling the critical defect size when manufacturing aluminum parts using PBF-LB. Moreover, investigations on the influence of pores and porosity on crack initiation and crack propagation will be helpful for the assessment of defects in large parts.

Appendix

A1: Experimental data for the tensile tests

Specimen	Ultimate tensile strength in MPa	Elongation at break in %
HD 1	420	5.5
HD 2	423	6.1
HD 3	415	5.3
HD 4	430	7.0
HD 5	435	7.6
KH 1	374	5.5
KH 2	393	6.7
KH 3	403	7.6
KH 4	402	7.7
KH 5	392	6.5
LoF 1	273	2.4
LoF 2	239	1.5
LoF 3	266	2.1
LoF 4	253	1.7
LoF 5	282	2.0

A2: Experimental data for the fatigue test

High-density specimens		Keyhole specimens		Lack of fusion specimens	
Stress amplitude in MPa	Load cycles	Stress amplitude in MPa	Load cycles	Stress amplitude in MPa	Load cycles
60	10,000,000	80	10,000,000	20	203,400
70	1,423,900	85	6,574,900	30	317,500
80	290,300	90	144,100	40	118,000
85	795,000	95	259,900	45	110,500
90	118,600	100	55,700	50	37,400
100	119,800	105	115,700	55	89,700
105	86,900	110	80,700	60	48,700
115	43,800	120	139,200	70	19,700
120	99,900	140	75,200	80	13,100
130	25,700	150	42,400		

Acknowledgements The presented work was funded by the Ministry of Science, Research and the Arts of the Federal State of Baden-Wuerttemberg within the 'InnovationCampus Future Mobility', which is gratefully acknowledged.

Funding Open Access funding enabled and organized by Projekt DEAL. This work was funded by Ministry of Science, Research and the Arts of the Federal State of Baden-Wuerttemberg.

Data availability The data supporting the findings of this study are available from the corresponding author upon request.

Declarations

Conflict of interest For this research, there is no conflict of interest for all authors.

References

1. Nicoletto G, Gallina L, Riva E (2019) Influence of as-built surfaces on the fatigue behavior of AlSi10Mg parts obtained by laser powder bed fusion. Proc Struct Integrity 24:381–389. https://doi.org/10.1016/j.prostr.2020.02.035
2. Tradowsky U, White J, Ward RM et al (2016) Selective laser melting of AlSi10Mg: influence of post-processing on the microstructural and tensile properties development. Mater Des 105:212–222. https://doi.org/10.1016/j.matdes.2016.05.066
3. Saravana Kumar M, Mohan E, Robinson S et al (2022) Comparative study on morphological, physical and mechanical characteristics of L-PBF based AlSi10Mg parts with conventional stir casted Al-10 %SiC composites. SILICON 14:2695–2706. https://doi.org/10.1007/s12633-021-01065-9
4. Afroz L, Das R, Qian M et al (2022) Fatigue behaviour of laser powder bed fusion (L-PBF) Ti–6Al–4V, Al–Si–Mg and stainless steels: a brief overview. Int J Fract 235:3–46. https://doi.org/10.1007/s10704-022-00641-3
5. Sajedi Z, Casati R, Poletti MC et al (2021) Comparative thermal fatigue behavior of AlSi7Mg alloy produced by L-PBF and sand casting. Int J Fatigue 152:106424. https://doi.org/10.1016/j.ijfatigue.2021.106424
6. Olakanmi EO, Cochrane RF, Dalgarno KW (2015) A review on selective laser sintering/melting (SLS/SLM) of aluminium alloy powders: processing, microstructure, and properties. Prog Mater Sci 74:401–477. https://doi.org/10.1016/j.pmatsci.2015.03.002
7. Zhao L, Song L, Santos Macías JG et al (2022) Review on the correlation between microstructure and mechanical performance for laser powder bed fusion AlSi10Mg. Addit Manuf 56:102914. https://doi.org/10.1016/j.addma.2022.102914
8. Raja A, Cheethirala SR, Gupta P et al (2022) A review on the fatigue behaviour of AlSi10Mg alloy fabricated using laser powder bed fusion technique. J Mater Res Technol 17:1013–1029. https://doi.org/10.1016/j.jmrt.2022.01.028
9. Pal R, Basak A (2022) Linking powder properties, printing parameters, post-processing methods, and fatigue properties in additive manufacturing of AlSi10Mg. Alloys 1:149–179. https://doi.org/10.3390/alloys1020010
10. Li W, Li S, Liu J et al (2016) Effect of heat treatment on AlSi10Mg alloy fabricated by selective laser melting: microstructure evolution, mechanical properties and fracture mechanism. Mater Sci Eng A 663:116–125. https://doi.org/10.1016/j.msea.2016.03.088
11. Lehner P, Blinn B, Zhu T et al (2024) Influence of the as-built surface and a T6 heat treatment on the fatigue behavior of additively manufactured AlSi10Mg. Int J Fatigue 187:108479. https://doi.org/10.1016/j.ijfatigue.2024.108479
12. Aboulkhair NT, Maskery I, Tuck C et al (2016) Improving the fatigue behaviour of a selectively laser melted aluminium alloy: influence of heat treatment and surface quality. Mater Des 104:174–182. https://doi.org/10.1016/j.matdes.2016.05.041
13. Konecna R, Uriati F, Nicoletto G et al (2021) Surface quality and fatigue behavior of L-PBF AlSi10Mg in as-built condition. Proc Struct Integrity 34:135–140. https://doi.org/10.1016/j.prostr.2021.12.020
14. Fini S, Croccolo D, de Agostinis M et al (2025) Fatigue response of AlSi10Mg by laser powder bed fusion: influence of build orientation, heat, and surface treatments. Prog Addit Manuf 10:1385–1403. https://doi.org/10.1007/s40964-024-00712-y
15. Nicoletto G (2020) Influence of rough as-built surfaces on smooth and notched fatigue behavior of L-PBF AlSi10Mg. Addit Manuf 34:101251. https://doi.org/10.1016/j.addma.2020.101251
16. Sajadi F, Tiemann J-M, Bandari N et al (2021) Fatigue improvement of AlSi10Mg fabricated by laser-based powder bed fusion through heat treatment. Metals 11:683. https://doi.org/10.3390/met11050683
17. Beretta S, Patriarca L, Gargourimotlagh M et al (2022) A benchmark activity on the fatigue life assessment of AlSi10Mg components manufactured by L-PBF. Mater Des 218:110713. https://doi.org/10.1016/j.matdes.2022.110713
18. Bao J, Wu Z, Wu S et al (2022) The role of defects on tensile deformation and fracture mechanisms of AM AlSi10Mg alloy at room temperature and 250 °C. Eng Fract Mech 261:108215. https://doi.org/10.1016/j.engfracmech.2021.108215
19. Jiang Z, Sun J, Berto F et al (2023) Fatigue and fracture behavior of AlSi10Mg manufactured by selective laser melting: a review. Phys Mesomech 26:367–390. https://doi.org/10.1134/S102995992304001X
20. Tusher MMH, Ince A (2023) A systematic review on high cycle and very high cycle fatigue behavior of laser powder bed fused (L-PBF) Al-Si alloys. Eng Fail Anal 154:107667. https://doi.org/10.1016/j.engfailanal.2023.107667
21. Afroz L, Qian M, Forsmark J et al (2025) Fatigue life of laser powder bed fusion (L-PBF) AlSi10Mg alloy: effects of surface roughness and porosity. Prog Addit Manuf 10:2423–2441. https://doi.org/10.1007/s40964-024-00759-x
22. Sausto F, Carrion PE, Shamsaei N et al (2022) Fatigue failure mechanisms for AlSi10Mg manufactured by L-PBF under axial and torsional loads: the role of defects and residual stresses. Int J Fatigue 162:106903. https://doi.org/10.1016/j.ijfatigue.2022.106903
23. Strauß L, Löwisch G (2024) Effect of residual stress, surface roughness, and porosity on fatigue life of PBF-LB AlSi10Mg. In: Altenbach H, Hitzler L, Johlitz M et al (eds) Lectures notes on advanced structured materials. Springer Nature Switzerland, Cham, pp 275–290
24. Du C, Zhao Y, Jiang J et al (2023) Pore defects in laser powder bed fusion: formation mechanism, control method, and perspectives. J Alloys Compd 944:169215. https://doi.org/10.1016/j.jallcom.2023.169215

25. Giovagnoli M, Silvi G, Merlin M et al (2021) Optimisation of process parameters for an additively manufactured AlSi10Mg alloy: limitations of the energy density-based approach on porosity and mechanical properties estimation. Mater Sci Eng A 802:140613. https://doi.org/10.1016/j.msea.2020.140613
26. Read N, Wang W, Essa K et al (2015) Selective laser melting of AlSi10Mg alloy: process optimisation and mechanical properties development. Mater Des 1980–2015(65):417–424. https://doi.org/10.1016/j.matdes.2014.09.044
27. Hastie JC, Kartal ME, Carter LN et al (2020) Classifying shape of internal pores within AlSi10Mg alloy manufactured by laser powder bed fusion using 3D X-ray micro computed tomography: influence of processing parameters and heat treatment. Mater Charact 163:110225. https://doi.org/10.1016/j.matchar.2020.110225
28. Bayat M, Thanki A, Mohanty S et al (2019) Keyhole-induced porosities in laser-based powder bed fusion (L-PBF) of Ti6Al4V: high-fidelity modelling and experimental validation. Addit Manuf 30:100835. https://doi.org/10.1016/j.addma.2019.100835
29. Thijs L, Kempen K, Kruth J-P et al (2013) Fine-structured aluminium products with controllable texture by selective laser melting of pre-alloyed AlSi10Mg powder. Acta Mater 61:1809–1819. https://doi.org/10.1016/j.actamat.2012.11.052
30. Weingarten C, Buchbinder D, Pirch N et al (2015) Formation and reduction of hydrogen porosity during selective laser melting of AlSi10Mg. J Mater Process Technol 221:112–120. https://doi.org/10.1016/j.jmatprotec.2015.02.013
31. Aboulkhair NT, Simonelli M, Parry L et al (2019) 3D printing of aluminium alloys: additive manufacturing of aluminium alloys using selective laser melting. Prog Mater Sci 106:100578. https://doi.org/10.1016/j.pmatsci.2019.100578
32. Yang KV, Rometsch P, Jarvis T et al (2018) Porosity formation mechanisms and fatigue response in Al-Si-Mg alloys made by selective laser melting. Mater Sci Eng A 712:166–174. https://doi.org/10.1016/j.msea.2017.11.078
33. Kan WH, Gao M, Zhang X et al (2022) The influence of porosity on Ti-6Al-4V parts fabricated by laser powder bed fusion in the pursuit of process efficiency. Int J Adv Manuf Technol 119:5417–5438. https://doi.org/10.1007/s00170-021-08374-8
34. Gong H, Rafi K, Gu H et al (2015) Influence of defects on mechanical properties of Ti–6Al–4V components produced by selective laser melting and electron beam melting. Mater Des 86:545–554. https://doi.org/10.1016/j.matdes.2015.07.147
35. Louvis E, Fox P, Sutcliffe CJ (2011) Selective laser melting of aluminium components. J Mater Process Technol 211:275–284. https://doi.org/10.1016/j.jmatprotec.2010.09.019
36. Strauß L, Löwisch G (2024) Prediction of fatigue lifetime and fatigue limit of aluminum parts produced by PBF-LB/M using a statistical defect distribution. Prog Addit Manuf 9:1299–1308. https://doi.org/10.1007/s40964-024-00577-1
37. Tang M, Pistorius PC (2017) Oxides, porosity and fatigue performance of AlSi10Mg parts produced by selective laser melting. Int J Fatigue 94:192–201. https://doi.org/10.1016/j.ijfatigue.2016.06.002
38. Murakami Y (2019) Metal fatigue: effects of small defects and nonmetallic inclusions, 2nd edn. Elsevier, Academic Press, London
39. El Haddad MH, Topper TH, Smith KN (1979) Prediction of non propagating cracks. Eng Fract Mech. https://doi.org/10.1016/0013-7944(79)90081-X
40. Romano S, Brückner-Foit A, Brandão A et al (2018) Fatigue properties of AlSi10Mg obtained by additive manufacturing: defect-based modelling and prediction of fatigue strength. Eng Fract Mech 187:165–189. https://doi.org/10.1016/j.engfracmech.2017.11.002
41. Strauß L, Duarte L, Kruse J et al (2025) An equivalent stress approach for predicting fatigue behavior of additively manufactured AlSi10Mg. Prog Addit Manuf 10:3071–3086. https://doi.org/10.1007/s40964-025-00974-0
42. Afazov S, Serjouei A, Hickman GJ et al (2023) Defect-based fatigue model for additive manufacturing. Prog Addit Manuf 8:1059–1066. https://doi.org/10.1007/s40964-022-00376-6
43. Afroz L, Inverarity SB, Qian M et al (2024) Analysing the effect of defects on stress concentration and fatigue life of L-PBF AlSi10Mg alloy using finite element modelling. Prog Addit Manuf 9:341–359. https://doi.org/10.1007/s40964-023-00457-0
44. DIN-Normenausschuss Feinmechanik und Optik (2021) Lasers and laser-related equipment – test methods for laser beam widths, divergence angles and beam propagation ratios – part 2: general astigmatic beams 31.260(DIN EN ISO 11146–2)
45. Wexel H, Kramer S, Schubert J et al (2024) Stream finishing of additively manufactured AlSi10Mg PBF-LB parts: influence on surface quality and fatigue behaviour. Proc CIRP 123:173–178. https://doi.org/10.1016/j.procir.2024.05.032
46. DIN-Normenausschuss Materialprüfung (2018) Testing of metallic materials – rotating bar bending fatigue test 77.040.10(DIN 50113)
47. DIN-Normenausschuss Materialprüfung (2022) Testing of metallic materials – tensile test pieces 77.040.10(DIN 50125)
48. DIN-Normenausschuss Materialprüfung (2022) Load controlled fatigue testing – execution and evaluation of cyclic tests at constant load amplitudes on metallic specimens and components 19.060; 77.040.10(DIN 50100)
49. Ji S, Gu Q, Xia B (2006) Porosity dependence of mechanical properties of solid materials. J Mater Sci 41:1757–1768. https://doi.org/10.1007/s10853-006-2871-9
50. Sert E, Hitzler L, Hafenstein S et al (2020) Tensile and compressive behaviour of additively manufactured AlSi10Mg samples. Prog Addit Manuf 5:305–313. https://doi.org/10.1007/s40964-020-00131-9
51. Brandl E, Heckenberger U, Holzinger V et al (2012) Additive manufactured AlSi10Mg samples using selective laser melting (SLM): microstructure, high cycle fatigue, and fracture behavior. Mater Des 34:159–169. https://doi.org/10.1016/j.matdes.2011.07.067
52. Tang M, Pistorius PC (2019) Fatigue life prediction for AlSi10Mg components produced by selective laser melting. Int J Fatigue 125:479–490. https://doi.org/10.1016/j.ijfatigue.2019.04.015
53. Delahaye J, Tchuindjang JT, Lecomte-Beckers J et al (2019) Influence of Si precipitates on fracture mechanisms of AlSi10Mg parts processed by selective laser melting. Acta Mater 175:160–170. https://doi.org/10.1016/j.actamat.2019.06.013
54. Xiong ZH, Liu SL, Li SF et al (2019) Role of melt pool boundary condition in determining the mechanical properties of selective laser melting AlSi10Mg alloy. Mater Sci Eng A 740–741:148–156. https://doi.org/10.1016/j.msea.2018.10.083
55. Streck S (2022) Algorithmus zur evaluierung des einflusses von porenclustern auf die lebensdauer von aluminiumdruckgusslegierungen. Karlsruher Institut für Technologie, Karlsruhe
56. Aigner R, Pusterhofer S, Pomberger S et al (2019) A probabilistic Kitagawa-Takahashi diagram for fatigue strength assessment of cast aluminium alloys. Mater Sci Eng A 745:326–334. https://doi.org/10.1016/j.msea.2018.12.108
57. Liu L, Wang S, Ma Y (2025) Rotating bending fatigue behavior of AlSi10Mg fabricated by powder bed fusion-laser beam: effect of layer thickness. Crystals 15:422. https://doi.org/10.3390/cryst15050422
58. Siddique S, Imran M, Walther F (2017) Very high cycle fatigue and fatigue crack propagation behavior of selective laser melted AlSi12 alloy. Int J Fatigue 94:246–254. https://doi.org/10.1016/j.ijfatigue.2016.06.003